New Journal of Physics
The open-access journal for physics

Laboratory and modeling studies of cloud–clear air interfacial mixing: anisotropy of small-scale turbulence due to evaporative cooling

Szymon P Malinowski[1,5], Miroslaw Andrejczuk[2], Wojciech W Grabowski[3], Piotr Korczyk[4], Tomasz A Kowalewski[4] and Piotr K Smolarkiewicz[3]

[1] Institute of Geophysics, University of Warsaw, Pasteura 7, 02-093 Warsaw, Poland
[2] Los Alamos National Laboratory, Los Alamos, NM, USA
[3] National Center for Atmospheric Research, Boulder, CO, USA
[4] Institute of Fundamental Technological Research, Polish Academy of Sciences, Warsaw, Poland
E-mail: malina@fuw.edu.pl

New Journal of Physics **10** (2008) 075020 (15pp)
Received 6 February 2008
Published 31 July 2008
Online at http://www.njp.org/
doi:10.1088/1367-2630/10/7/075020

Abstract. Small-scale mixing between cloudy air and unsaturated clear air is investigated in numerical simulations and in a laboratory cloud chamber. Despite substantial differences in physical conditions and some differences in resolved scales of motion, results of both studies indicate that small-scale turbulence generated through cloud–clear air interfacial mixing is highly anisotropic. For velocity fluctuations, numerical simulations and cloud chamber observations demonstrate that the vertical velocity variance is up to a factor of two larger than the horizontal velocity variance. The Taylor microscales calculated separately for the horizontal and vertical directions also indicate anisotropy of turbulent eddies. This anisotropy is attributed to production of turbulent kinetic energy (TKE) by buoyancy forces due to evaporative cooling of cloud droplets at the cloud–clear air interface. Numerical simulations quantify the effects of buoyancy oscillations relative to the values expected from adiabatic and isobaric mixing, standardly assumed in cloud physics. The buoyancy oscillations result from microscale transport of liquid water due to the gravitational sedimentation of cloud droplets. In the particular modeling setup considered here, these oscillations contribute to about a fifth of the total TKE production.

[5] Author to whom any correspondence should be addressed.

Contents

1. Introduction 2
2. Physics of cloud–clear air interfacial mixing 3
3. Numerical simulations of cloud–clear air interfacial mixing 5
4. Laboratory experiments with cloud–clear air interfacial mixing 10
5. Conclusions 13
Acknowledgments 14
References 14

1. Introduction

Properties of cloud turbulence at sub-centimetre scales, relevant to interactions between cloud droplets and air flow, have never been documented on the basis of *in situ* measurements. Turbulence in clouds is different than that observed in wind tunnels, because it covers a wider range of scales and has lower rate of turbulent kinetic energy (TKE) dissipation. Spatial scales of cloud turbulence span six decades in the range from millimetres up to hundreds of metres, compared to roughly three decades in wind tunnels. Reported mean values of the dissipation rate vary from as low as $10^{-5}\,\mathrm{m^2\,s^{-3}}$ up to about $10^{-1}\,\mathrm{m^2\,s^{-3}}$, depending on the cloud type, life-cycle stage and other factors [1, 2].

According to turbulence theories extending beyond the classical isotropic homogeneous Kolmogorov's model [3, 4], broadening of the range of spatial scales increases intermittency of the small-scale turbulence [5, 6]. In a recent work [2], the authors were able to measure *in situ* turbulent velocities in clouds at scales from hundreds of metres down to a few tens of centimetres, and they demonstrated fluctuations of TKE up to four orders of magnitude (see their figures 8 and 9). They reported a log-normal probability density distribution of the estimated TKE dissipation rate, spanning a range of ten decades. However, the smallest scales resolved in their measurements were still about two orders of magnitude larger than the typical distance between cloud droplets [7, 8]. Incidentally, the latter matches the Kolmogorov microscale for typical TKE values in clouds. This, interpreted in terms of a multifractal approach (cf section 6 of [6]), suggests that turbulence in clouds is even more intermittent at scales where interactions between droplets occur. In such a case, a relatively weak TKE source may influence turbulence on scales important for droplet–flow interactions.

In this paper, we discuss such a source of TKE, namely buoyancy forces resulting from the cooling due to evaporation of cloud droplets near the interface that separates cloud and clear air filaments. It is widely accepted that buoyancy reversal, due to cloud condensate evaporation during mixing of a cloudy air with unsaturated environment, affects large-scale cloud dynamics [9]–[12]. Here we show that the accompanying small-scale effects are important for statistical properties of turbulence. In particular, evaporative cooling near the interface leads to anisotropy of turbulence at scales close to the dissipation range.

The fundamental importance of small-scale mixing and turbulence in clouds cannot be overemphasized. It is well documented that the prevailing volume in clouds is affected by the entrainment and mixing. In other words, natural clouds do not adhere to a simple classical model of a homogeneous parcel ascending adiabatically in static environment. This holds both for convective cumuliform clouds [13, 14] as well as for stratiform clouds [15]. Combined effects of entrainment, mixing and evaporative cooling make the evolution of droplet spectra

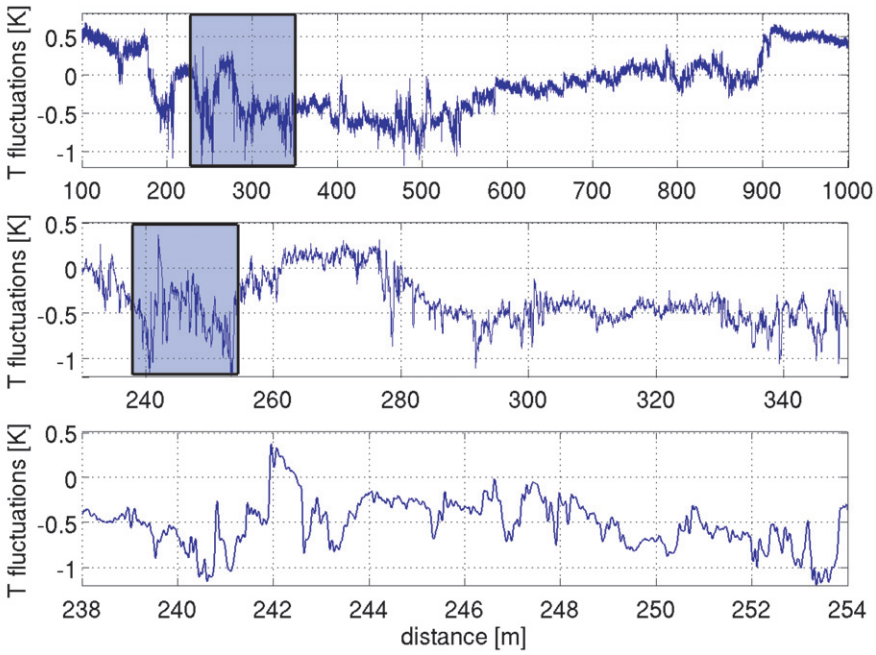

Figure 1. An example of the temperature time series recorded during aircraft penetration of a convective cloud. The rectangular areas marked in the upper and central plates are magnified, respectively, in the central and lower plates.

dependent not only on droplet inertia in turbulent airflow, but also on fine details of dilution and evaporation. In turn, due to latent cooling, the evaporation affects local air density. The resulting inhomogeneity of the spatial density distribution results in buoyant accelerations of air filaments, thus feeding back to the dynamics and turbulence. These fine-scale effects are typically neglected in larger-scale models. In this paper, we show that they may substantially influence the statistical properties of small-scale turbulence in clouds. Because the small-scale dynamics and thermodynamics underlie the evolution of droplet spectra—and, thus, radiative properties of clouds—the importance of the effects discussed can be argued up to the climatic scale.

The paper is organized as follows. The next section introduces the problem and presents *in situ* cloud observations, which demonstrate that a large fraction of a cloud volume is filamented due to entrainment and mixing events. Section 3 discusses results of numerical simulations of small-scale mixing between the cloudy and clear air, designed to study properties of small-scale turbulence produced by evaporative cooling of cloud droplets. Section 4 presents the laboratory experiment that mimics the cloud–clear air interfacial mixing and compares the results to numerical simulation. Section 5 concludes the paper.

2. Physics of cloud–clear air interfacial mixing

Consider an isobaric entrainment event initiated at the top or near the edge of a convective cloud. Such an event is typically associated with an eddy resulting from the instability of the cloud-environment boundary [16]–[18]. Once a parcel of unsaturated environmental air becomes engulfed by saturated cloudy air containing small water droplets, both volumes undergo stirring and filamentation in the process of turbulent mixing [13], [19]–[21]. This is illustrated in figure 1 that shows high-resolution temperature measurements taken by aircraft [22, 23]. The upper

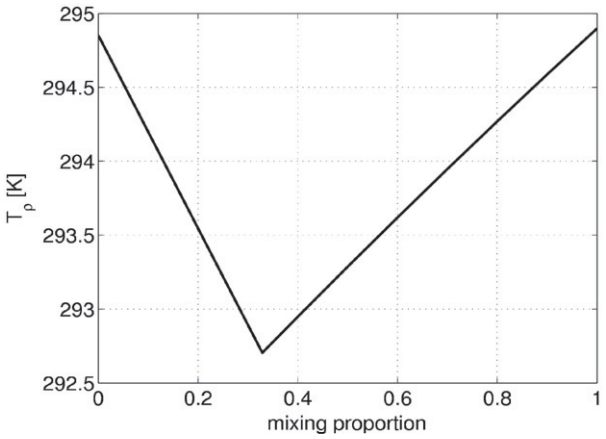

Figure 2. Density temperature of homogenized mixture of the environmental air (with 20 °C temperature and 65% relative humidity) and saturated cloudy air (with 20 °C temperature and 3.2 g kg^{-1} liquid water mixing ratio) as a function of the environmental air fraction.

panel shows the in-cloud temperature to be lower than that of the environment, in the range from 180 to 900 m. The two subsequent magnifications in the central and lower panels show discontinuities characteristic of passing through the filaments with different thermodynamic properties. Small-scale filaments, down to the centimetre scale (an instrumental limit) are apparent in the lower panel. Such measurements are typical for many cloud types and a variety of meteorological conditions [2, 22, 23]. Molecular diffusion of water vapor and temperature across the interface separating cloudy and clear air filaments, combined with the transport of cloud droplets from cloudy to clear air filaments due to droplet sedimentation and inertia, results in the evaporation of water within the clear air filaments [11], [24]–[26] during the stirring phase of the mixing (i.e. before the Kolmogorov scale is reached).

Evaporation of cloud droplets implies density changes due to latent heat effects. In order to illustrate the importance of these effects, figure 2 shows the dependence of the density temperature of the homogenized mixture (cf equation (4.3.6) in [27] and the discussion below) as a function of the environmental air fraction in the mixture (cf figure 1 in [11] and figure 5 in [26]). This figure is referred to as the mixing diagram. Mixing is assumed to be adiabatic and isobaric, a standard approximation for cloud processes. The density temperature T_ρ is often used in cloud physics to represent combined effects of the air temperature, water vapor and condensed water loading on the parcel density. It can be approximated as:

$$T_\rho = T\,(1+\varepsilon q - l)\,, \tag{1}$$

where T is the temperature, q is the water vapor mixing ratio, l is the liquid water (cloud droplet) mixing ratio, and $\varepsilon = (R_\mathrm{v}/R_\mathrm{d} - 1) \sim 0.61$; R_d and R_v are gas constants of dry air and water vapor, respectively. Values of thermodynamic parameters in figure 2 were selected to represent typical small summertime cumulus, and they satisfy the assumption of zero buoyancy of the cloudy air, selected for consistency with numerical simulations discussed later in the paper. The mixing diagram consists of two line segments, the common point of which represents a state where the homogenized mixture is at saturation and contains no cloud water. This is the mixture with the lowest density temperature, that is, with the largest density. The segment to the right of

the common point corresponds to the unsaturated, cloud-free homogenized mixtures, whereas the segment to the left corresponds to the saturated cloudy mixtures. The diagram shows that evaporation of liquid water due to mixing between cloudy air and the unsaturated environment results in a homogenized mixture that has lower density temperature (i.e. higher density) than either of the elements. Here, the minimum is for the mixing proportion of 33% environmental and 67% cloudy air.

The negative buoyancy created by the mixing results in production of TKE. For incompressible Boussinesq dynamics with triply periodic boundaries, it can be shown (see appendices in [17, 26]) that the TKE evolution satisfies:

$$\frac{\mathrm{d}}{\mathrm{d}t}\mathrm{TKE} = \langle u_3 b\rangle - 2\nu\langle\Omega\rangle, \tag{2}$$

where $\mathrm{TKE} = 1/2(\vec{u})^2$; $\vec{u} = (u_1, u_2, u_3)$ is the vector of turbulent velocity fluctuations (i.e. perturbations from time-dependent volume-averaged fields); $b = g(T_\rho/T_{\rho_0})$ is the buoyancy fluctuation, with T_ρ denoting fluctuation of the perturbation from the reference density temperature T_{ρ_0} and g the acceleration of gravity; $\Omega = 1/2\langle(\nabla\times\vec{u})^2\rangle$ is the enstrophy; ν is the molecular viscosity; and $\langle\,\rangle$ represents the volume averaging. The first term on the rhs of equation (2) represents production of the TKE through the correlations between fluctuations of the vertical velocity and buoyancy. The second term represents destruction of the TKE through viscous dissipation in regions of large velocity gradients (and thus of high enstrophy).

TKE can also be supplied at large scales. For instance, in the case of the entrainment event discussed at the beginning of this section, the kinetic energy associated with the entraining eddy provides a large-scale source of TKE. In numerical simulation, the large-scale source may be associated with the initial conditions (discussed in the next section). A particular setup of the laboratory experiment may provide a large-scale source of TKE as well (see section 4). In all these cases, the buoyant TKE production at small scales (i.e. the first term on rhs of equation (2)) supplements the TKE cascading from larger scales.

The buoyancy fluctuations in (2) may originate from evaporative cooling due to adiabatic and isobaric mixing between cloudy and clear-air illustrated in figure 2. However, as pointed out in [11] (see figure 3 therein and the accompanying discussion), sedimentation of droplets from cloudy to clear air filaments provides an additional transport mechanism for liquid water, which affects T_ρ by changes of l (and q in the case of evaporation) increasing in consequence the range of buoyancy fluctuations beyond that resulting from the adiabatic isobaric mixing. In [11], the author referred to such amplified negative fluctuations of b as the 'buoyancy undershoots'. Here, to accommodate both negative and positive extrema, we shall refer to such amplified fluctuations of b as 'buoyancy oscillations'. Numerical simulations discussed in the next section assess the role of these oscillations in the TKE budget.

3. Numerical simulations of cloud–clear air interfacial mixing

A large series of numerical simulations of cloud–clear air mixing set forth in the idealized scenario of decaying moist turbulence were discussed in [25, 26]. In these studies, the initial conditions included a set of randomly oriented cloudy and clear-air filaments as well as initial velocity perturbations, all dominated by features at scales comparable to the size of the computational domain (see figure 1 in [25]). The simulations investigated the evolution of cloud–clear air mixing and subsequent microscale homogenization, with emphasis on the TKE

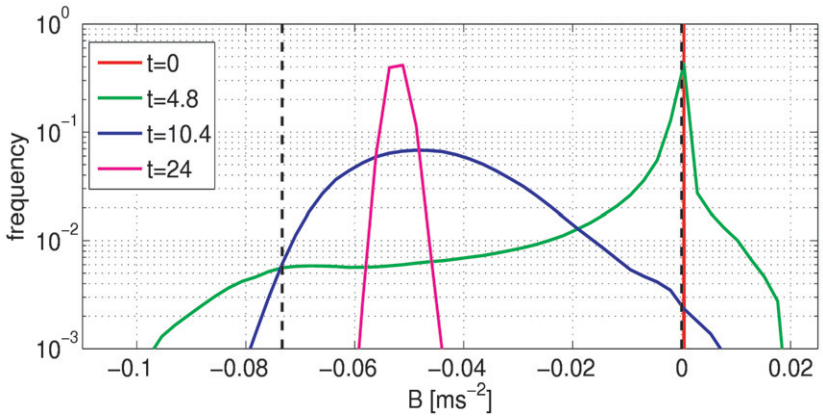

Figure 3. Histograms of buoyancy within the model domain at the beginning of calculations and at times of 4.8, 10.4 s and at the end of calculations (24 s). Dashed black lines show the range of buoyancy fluctuations due to isobaric and adiabatic mixing.

generation by evaporative cooling at the edges of cloudy filaments and on the role of droplet sedimentation in transport of cloud water across the cloud–clear air interface.

The finite-difference numerical model EULAG used in the simulations is described in [28]–[31]. The equations, modeling setup, initial and boundary conditions, as well as comprehensive discussion of various aspects of simulations, are presented in [25, 26]. Here, we focus on the results from the simulation of a mixing event in a triply periodic domain of (64 cm)^3 resolved with 256^3 grid (i.e. with grid increment of 2.5 mm). To represent the finite evaporation time of cloud droplets and a realistic spectrum of their sedimentation velocities, the cloud droplet number density was discretized using 16 size classes (bins). The resolution selected qualifies the calculations as DNS [32, 33] with a superimposed binned cloud microphysics [25, 26].

The initial temperature and relative humidity of the clear air were set at 293 K and 65%, respectively. Cloudy filaments were saturated, with their temperature the same as that of the clear air and the liquid water content (LWC) of 3.2 g kg^{-1}. The initial spectrum of cloud droplets was narrow, with the mean droplet radius of 8.9 μm and width of $\sim$1.5 μm, not atypical for natural clouds. The initial fraction of the volume occupied by cloudy filaments was 50%. The initial conditions were selected to assure identical density temperatures of cloudy filaments and clear air (figure 2), thus implying that all simulated buoyancy variations result from the sedimentation of cloud droplets relative to the air, and from the latent heating due to evaporation of cloud droplets. The imposed initial velocity perturbations result in the TKE of 1.62×10^{-4} m^2 s^{-2}, which corresponds to a weak turbulence [25, 26].

Figure 3 shows frequency distributions (histograms) of the buoyancy fluctuations at selected times. Black dashed lines show the limits of the adiabatic isobaric mixing illustrated in figure 2. The initial ($t = 0$ s) delta distribution at vanishing fluctuations reflects identical values of the density temperatures of cloudy and clear-air filaments.

At $t = 4.8$ s, when the buoyant TKE production is the most intense, the histogram is very wide, exceeding the limits of adiabatic isobaric mixing. Positive buoyancy oscillations, to the right of the upper limit in figure 3, occur in cloudy saturated regions with LWC reduced by droplet sedimentation (i.e. resulting from the decrease of l in equation (1)). Negative oscillations

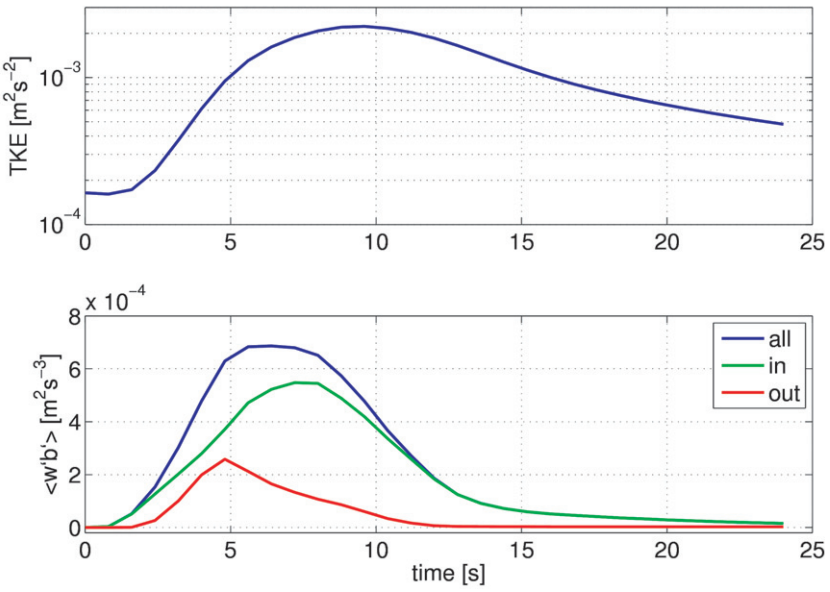

Figure 4. Evolution of the volume-averaged TKE (upper panel) and its buoyant production (lower panel, blue line); contributions to the buoyant production by buoyancy fluctuations within and outside the limits resulting from isobaric and adiabatic mixing are shown in green and red lines, respectively.

(corresponding to buoyancy undershoots) occur in subsaturated regions due to latent cooling associated with evaporation of cloud droplets sedimenting from cloudy filaments (see [11] for a detailed discussion). As time progresses, the histograms narrow, to eventually converge to a delta distribution corresponding to the buoyancy of the homogenized mixture. As the histogram shows at $t = 24$ s, at the end of the simulation the homogenized state is not yet achieved.

Figure 4 documents the TKE evolution in the course of the simulation (upper panel) and the buoyant TKE production (lower panel). TKE increases rapidly in the first 5 s, and more gradually in the following few seconds, to reach the maximum value of 2.2×10^{-3} m^2 s^{-2} in the 9th second. Subsequently, TKE gradually decreases due to prevailing dissipation. After 24 s, at the end of the simulation, TKE is still about three times larger than its initial value. The bottom panel of figure 4 shows the partition of the TKE production from regions where the buoyancy fluctuations fall within the limits set by the adiabatic isobaric mixing (green line, marked 'in') and regions where the buoyancy exceeds these limits (red line, marked as 'out').

Furthermore, figure 4 shows that TKE production during the initial stages of mixing is divided about equally between regions with buoyancy values within the limits of the classical mixing (figure 2) and regions with buoyancy oscillations. Although the contribution of these oscillations to the TKE budget diminishes at later stages (when TKE is mostly dissipated), they provide about 20% of the total TKE production for the entire simulation.

The anisotropy of the velocity field develops during the first 5 s of the simulation, when the TKE increases rapidly. This is illustrated in figure 5 in two ways. Firstly, the upper panel shows the evolution of the ratio of the root mean square (rms) values of turbulent velocity fluctuations in the horizontal and vertical $\langle u_i^2 \rangle / \langle u_3^2 \rangle$ ($i = 1$ and 2 refer to the two horizontal directions). Secondly, the lower panel presents the evolution of the Taylor microscales based on

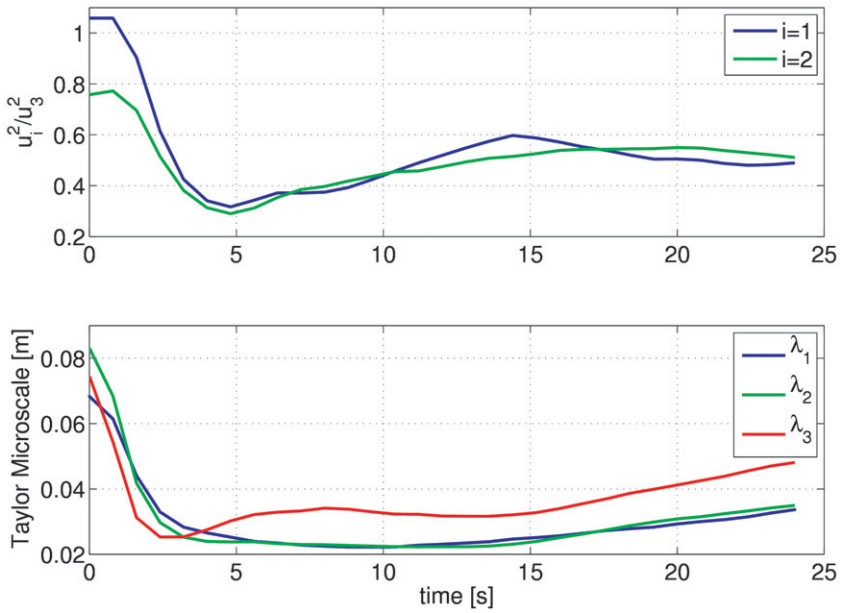

Figure 5. Evolution of the ratios $\langle u_i^2\rangle/\langle u_3^2\rangle$ (upper panel) and of the Taylor microscales (lower panel). Anisotropy in the first second of the simulation is due to that of the initial condition [34].

the horizontal and vertical velocity components, defined as:

$$\lambda_i = \frac{\langle u_i^2\rangle^{1/2}}{\langle(\partial u_i/\partial x_i)^2\rangle^{1/2}}. \tag{3}$$

The ratios $\langle u_i^2\rangle/\langle u_3^2\rangle$ decrease rapidly in the first seconds of simulation. Their minima, of about 0.33, are reached at the time of the maximum TKE production around the 4th second. Then, the ratios increase slightly, as the TKE evolution levels off, and settle down at values close to 0.5 for the remainder of the simulation. The anisotropy persists, even at the very end of the simulation when TKE gradually decreases due to dissipation. This anisotropy of the small-scale turbulence is also corroborated by the differences in the Taylor microscales [25]. Evolution of the two horizontal scales λ_1 and λ_2 and of the vertical scale λ_3 is shown in the bottom panel. From the 5th second of the simulation onward, $\lambda_3$is significantly larger than λ_1 and λ_2.

Figure 6 shows histograms of velocity fluctuations at various times of the simulation. Statistical properties of the results displayed in the histograms are summarized in table 1. In the first histogram ($t = 4.8$ s), corresponding to increasing TKE production and the maximum effect of buoyancy oscillations in figure 4, the histograms are narrow, skewed and of high kurtosis. Next, histograms show (approximately) Gaussian shapes, with amplified widths concomitant with the enhanced TKE values. Consistent with the results of figure 5, the spread of the vertical velocity histograms is significantly wider than the spread of the horizontal velocity histograms.

Figure 7 illustrates the discussion with a snapshot of the LWC field in the vertical cross section through the computational domain at $t = 10.8$ s, that is, around the time of maximal TKE. The figure shows some filaments elongated in the vertical—documented in the objective analysis reported in [24, 35]—most likely due to the increased vertical strain associated with enhanced vertical velocities.

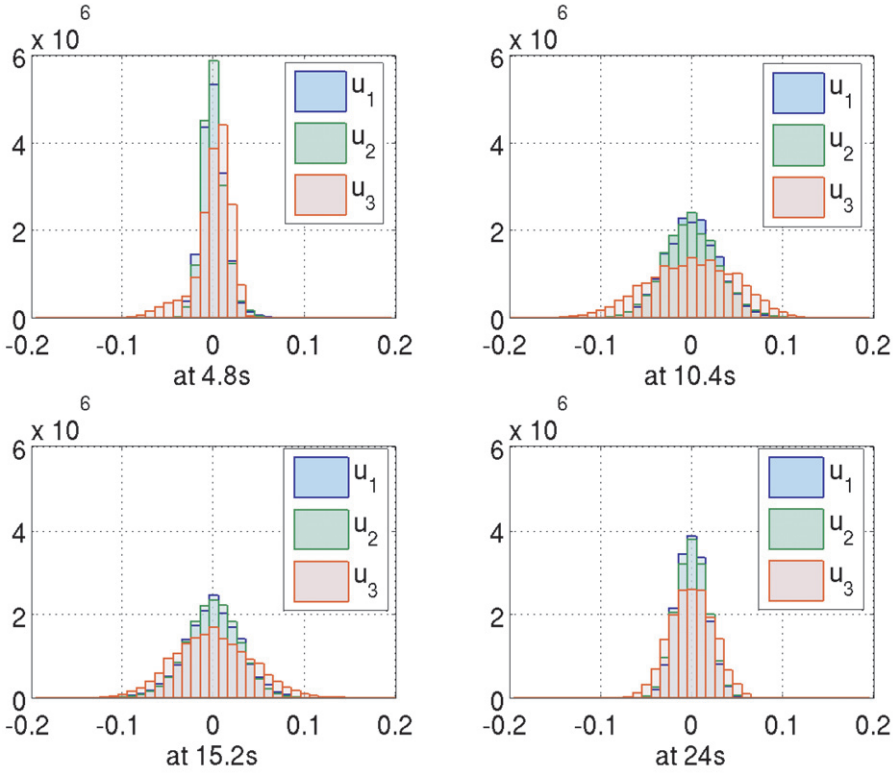

Figure 6. Histograms of velocity fluctuations at 4.8, 10.4, 15.2 s and at the end of the simulation.

Table 1. Distribution of horizontal (u_1, u_2) and vertical (u_3) turbulent velocity fluctuations in selected times from the beginning of calculations.

	Time (s)	Standard deviation (cm s^{-1})	Skewness	Kurtosis
u_1	4.8	1.59	0.79	5.2
u_2	4.8	1.52	0.76	5.1
u_3	4.8	2.73	−1.64	6.1
u_1	10.4	3.19	0.01	3.3
u_2	10.4	3.23	−0.03	3.2
u_3	10.4	4.69	0.13	2.9
u_1	15.2	3.19	−0.07	3.3
u_2	15.2	3.09	−0.13	3.3
u_3	15.2	4.56	0.15	3.0
u_1	24	1.66	0.14	2.9
u_2	24	1.74	0.06	2.9
u_3	24	2.39	−0.05	2.8

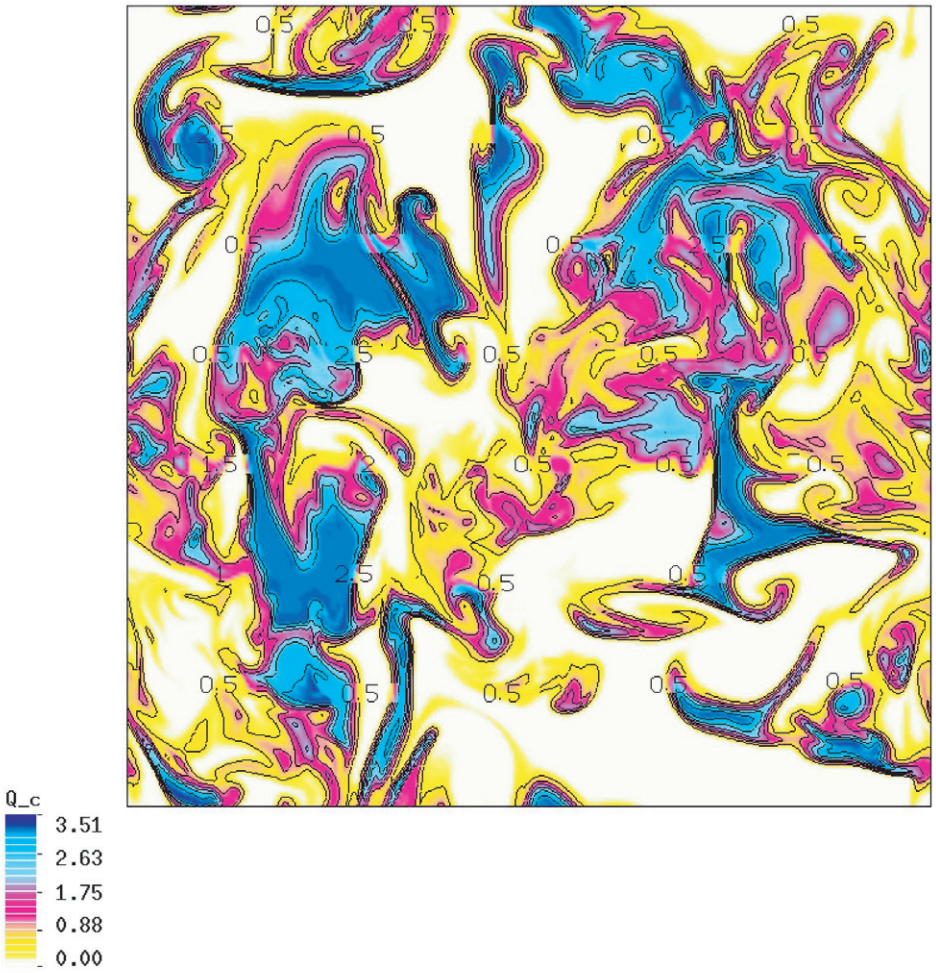

Figure 7. LWC (Q_c) in a vertical cross section through the computational domain after 10.8 s of the simulation. The area of the cross section is 64 cm × 64 cm, and white regions represent clear air filaments.

4. Laboratory experiments with cloud–clear air interfacial mixing

Our experiments mimic small-scale processes of turbulent mixing of cloudy air with unsaturated environmental air in a laboratory cloud chamber (1.0 m × 1.0 m × 1.8 m, figure 8, [36]). A saturated and cloudy plume (containing droplets of ∼10 μm diameter) enters the chamber through the round opening in the ceiling. The velocity of the plume is about 20 cm s^{-1} at the inlet, and it accelerates to about 30 cm s^{-1} in the middle of the chamber in response to the buoyancy forces. LWC in the plume is typically more than 10 g kg^{-1}—somewhat higher than in natural clouds. The plume's temperature is about 25 °C, close to the temperature of the unsaturated chamber air. Relative humidity of the clear air inside the chamber varies from 30 to 75% for different experiments. The plume descends through the chamber while mixing with the environment, creating complicated continuously evolving structures (eddies, filaments, etc).

Illuminating the chamber interior with a 1.2 mm thick sheet of laser light enables the planar cross section through the scene to be imaged with a high-resolution CCD camera. An example

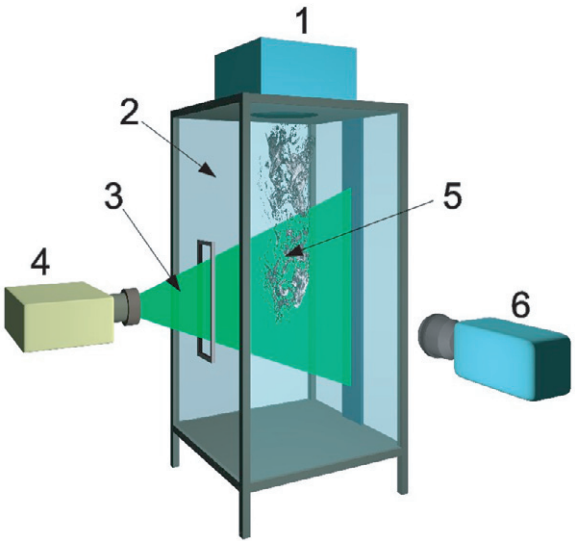

Figure 8. Laboratory setup: (1) small container filled with cloudy air, (2) mixing chamber, (3) laser light sheet, (4) double-pulse laser, (5) cloudy plume undergoing mixing, and (6) CCD camera.

image from the experiment, covering an area of about $9 \times 6\,\mathrm{cm}^2$, is presented in figure 9. The image reveals fine structures created in the process of turbulent mixing of the cloudy plume with its unsaturated environment. One pixel in this image corresponds to the 1.2 mm deep volume with about $69 \times 69\,\mu\mathrm{m}^2$ area in the plane of the laser-light sheet. Such elementary volumes occupied by droplets are represented by dark pixels in the image; bright pixels correspond to volumes void of droplets.

Pattern recognition in two consecutive images separated by a known time interval allows retrieval of two velocity components in the image plane. This technique, referred to as particle image velocimetry (PIV) [37], is widely adopted in experimental fluid mechanics. An original, accurate multi-scale PIV algorithm was developed for this experiment [36]. First, it identifies motions of large structures, and then analyzes the displacements within the structures. Application of the algorithm allows the two components of velocity vector to be estimated with a spatial resolution of about 0.07 mm; i.e. an order of magnitude smaller than the Kolmogorov length scale, the value of which was estimated from the measurements at approximately 0.76 mm. An example image showing a pattern of droplets superimposed with the retrieved two velocity components is shown in figure 10.

In the preliminary experiment described in [36], only 20 scenes allowed PIV velocity retrievals. These were collected at lower LWC of the plume ($\sim 4\,\mathrm{g\,kg}^{-1}$) implying a smaller potential for evaporative cooling, and thus lower values of TKE. The observed ratio of $\langle u_1'^2 \rangle / \langle u_3'^2 \rangle$ was estimated as 0.67 ± 0.52, that is, with a large uncertainty. Other statistics, like the horizontal and vertical Taylor microscales, showed anisotropy as well, but the experimental errors were high. Here, we present a new set of results that extend the discussion of [36]. The data were collected in a series consisting of 20 experiments, each subject to slightly different thermodynamic conditions inside the chamber. For each experiment, at least 100 pairs of frames (tens of thousands of velocity vectors in each frame) were analyzed, in order to retrieve statistical properties of velocity fluctuations. Experimental probability distribution functions (PDF) of the velocity fluctuations in horizontal (u_1') and vertical (u_3') directions are presented

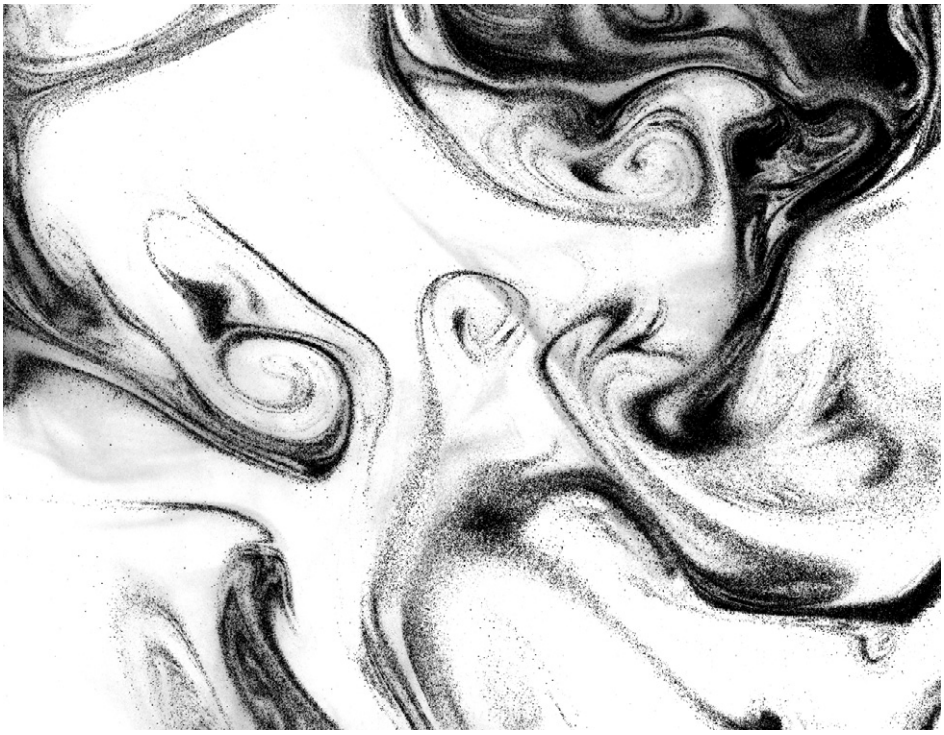

Figure 9. An example image from the cloud chamber. Dark pixels are occupied by cloud droplets. Image covers a physical area of $\sim 9 \times 6\,\mathrm{cm}^2$.

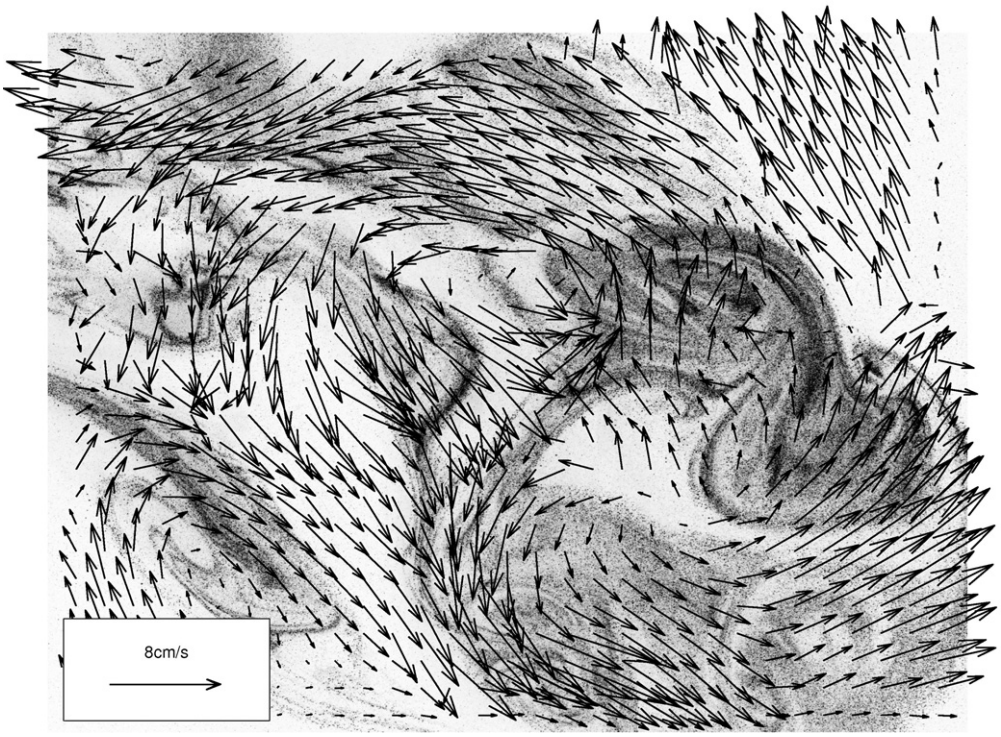

Figure 10. An example of two-dimensional velocity fluctuations retrieved from a pair of consecutive images using the multi-scale PIV algorithm.

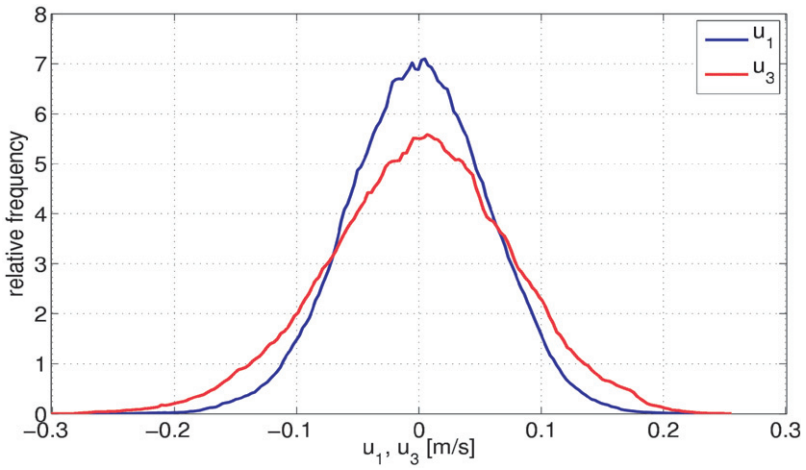

Figure 11. Composite distribution of horizontal (blue) and vertical (red) velocity fluctuations retrieved from a series of 20 laboratory experiments.

Table 2. Average distribution of horizontal (u_1') and vertical (u_3') turbulent velocity fluctuations from 20 experiments.

	Standard deviation ($\mathrm{cm\,s^{-1}}$)	Skewness	Kurtosis
u_1'	5.4	−0.01	3.2
u_3'	8.0	−0.2	3.1

in figure 11 and summarized in table 2. Clearly, the PDF of u_3' is wider and has longer tails than the PDF of u_1', consistent with the numerical simulation discussed in the preceding section. The derived kurtosis and skewness indicate that both the distributions are close to Gaussian. The ratio $\langle u_1'^2\rangle/\langle u_3'^2\rangle = 0.46 \pm 0.07$ (a mean over all 20 experiments) is, again, consistent with the numerical simulation. Mean Taylor microscales, estimated independently for horizontal (λ_1) and vertical (λ_3) velocity components, are 7.5 ± 0.4 and 9.2 ± 0.6 mm, respectively. These values, obtained from measurements resolving smallest scales of the flow, also indicate anisotropy.

The anisotropy in the laboratory experiments is most likely the result of evaporative cooling at the cloud–clear air interface, but the impact of the large-scale anisotropy of the experimental setup (i.e. the initial plume being injected from the top of the chamber) cannot be ruled out. This is corroborated by additional experiments using the same laboratory setup, but with non-evaporating oil droplets replacing cloud water [38]. The observed $\langle u_1'^2\rangle/\langle u_3'^2\rangle$ ratio in these experiments was 0.86 ± 0.02, suggesting small but non-negligible impact of the experimental setup and/or buoyancy oscillations (due to weight of oil droplets) on the observed small-scale anisotropy.

5. Conclusions

Results of laboratory experiments and numerical simulations show that evaporative cooling and droplet sedimentation in the vicinity of the cloud–clear air interface lead to the anisotropy of

small-scale turbulence associated with cloud entrainment and mixing. In spite of the substantial variability in thermodynamic conditions between different series of measurements in the mixing chamber, and in spite of inevitable simplifications adopted in the numerical simulation, the overall agreement of results is remarkable. In particular, the ratio between the horizontal and vertical velocity variance is approximately 0.5 in both numerical and laboratory experiments. We also show that a non-negligible amount of TKE (20% in the current study) originates from processes dismissed in classical theory of cloud–clear air mixing; that is, from small-scale buoyancy oscillations. These oscillations result from different microscale transport mechanisms, across the cloud–clear air interface, of the temperature and water vapor (via molecular diffusion) and of cloud droplets (via sedimentation).

In contrast to the extrapolations of *in situ* measurements that suggest homogeneity and isotropy of cloud turbulence at tens-of-metres down to decimetre scales, our findings indicate that the anisotropy at the cloud microscale is independent of the larger scales. As pointed out in the introduction, the reported anisotropy of small scales due to turbulent entrainment and mixing, combined with the well-known fact that clouds are strongly diluted by entrainment, leads us to believe that the effects discussed in this paper may have significant implications for radiative transfer through clouds and for growth of cloud droplets through collision/coalescence. Theoretical models of such processes typically assume random distribution of droplets in space, which is clearly not the case when turbulent cloud–clear air mixing is considered. Implications of such approximations need to be investigated in the future.

Acknowledgments

This work was supported by the Polish Ministry of Science and Higher Education and inspired by the International Collaboration for Turbulence Research (ICTR). NCAR is sponsored by the National Science Foundation. PKS acknowledges partial support from the USA Department of Energy CCPP and SciDAC research programs while conducting this work.

References

[1] MacPherson J I and Isaac G A 1977 *J. Appl. Meteorol.* **16** 81–90
[2] Siebert H, Lehmann K and Wendisch M 2006 *J. Atmos. Sci.* **63** 1451–66
[3] Frisch U 1996 *Turbulence: The Legacy of A N Kolmogorov* (Cambridge: Cambridge University Press)
[4] Tsinober A 2001 *An Informal Introduction to Turbulence* (Berlin: Springer)
[5] Sreenivasan K R and Antonia R A 1997 *Annu. Rev. Fluid. Mech.* **29** 435–72
[6] Sreenivasan K R 2004 *Flow Turbul. Combust.* **72** 115–31
[7] Brenguier J-L 1993 *J. Appl. Meteorol.* **32** 783–93
[8] Lehmann K, Siebert H, Wendisch M and Shaw R A 2007 *Tellus* B **59** 57–65
[9] Deardorff J W 1980 *J. Atmos. Sci.* **37** 131–47
[10] Randall D A 1980 *J. Atmos. Sci.* **37** 125–30
[11] Grabowski W W 1993 *Q. J. R. Meteorol. Soc.* **119** 935–56
[12] Lock A P and MacVean M K 1999 *Q. J. R. Meteorol. Soc.* **125** 1017–38
[13] Paluch I R and Baumgardner D G 1989 *J. Atmos. Sci.* **46** 261–78
[14] Blyth A M 1993 *J. Appl. Meteorol.* **32** 626–41
[15] Gerber H, Frick G, Malinowski S P, Brenguier J-L and Burnet F 2005 *J. Atmos. Sci.* **62** 443–59
[16] Klaassen G P and Clark T L 1985 *J. Atmos. Sci.* **42** 2621–42
[17] Grabowski W W and Clark T L 1991 *J. Atmos. Sci.* **48** 527–46

[18] Grabowski W W and Clark T L 1993 *J. Atmos. Sci.* **50** 555–73
[19] Baker B A 1992 *J. Atmos. Sci.* **49** 387–404
[20] Malinowski S P and Zawadzki I 1993 *J. Atmos. Sci.* **50** 5–13
[21] Broadwell J E and Breidenthal R E 1982 *J. Fluid Mech.* **125** 397–410
[22] Haman K E and Malinowski S P 1996 *Atmos. Res.* **41** 161–75
[23] Haman K E, Malinowski S P, Kurowski M J, Gerber H and Brenguier J-L 2007 *Q. J. R. Meteorol. Soc.* **133** 213–26
[24] Malinowski S P, Zawadzki I and Banat P 1998 *J. Atmos. Ocean. Technol.* **15** 1060–5
[25] Andrejczuk M, Grabowski W W, Malinowski S P and Smolarkiewicz P K 2004 *J. Atmos. Sci.* **61** 1726–39
[26] Andrejczuk M, Grabowski W W, Malinowski S P and Smolarkiewicz P K 2006 *J. Atmos. Sci.* **63** 3204–25
[27] Emmanuel K A 1994 *Atmospheric Convection* (Oxford: Oxford University Press)
[28] Smolarkiewicz P K and Margolin L G 1997 *Atmos.–Ocean* **35** 127–52
[29] Smolarkiewicz P K and Margolin L G 1998 *J. Comput. Phys.* **140** 459–80
[30] Grabowski W W and Smolarkiewicz PK 1990 *Mon. Weather Rev.* **118** 2082–97
[31] Grabowski W W and Smolarkiewicz P K 2002 *Mon. Weather Rev.* **130** 939–56
[32] Domaradzki J A, Xiao Z and Smolarkiewicz P K 2003 *Phys. Fluids* **15** 3890–3
[33] Margolin L G, Smolarkiewlcz P K and Wyszogrodzki A A 2006 *J. Appl. Mech. ASME* **73** 469–73
[34] Herring J R and Kerr R M 1993 *Phys. Fluids.* A **5** 2792–8
[35] Banat P and Malinowski S P 1999 *Phys. Chem. Earth.* B **24** 741–5
[36] Korczyk P M, Malinowski S P and Kowalewski T A 2006 *Atmos. Res.* **82** 173–82
[37] Raffel M, Willert Ch E and Kompenhans J 2002 *Particle Image Velocimetry: A Practical Guide* 2nd edn (Berlin: Springer)
[38] Korczyk P 2008 Effect of cloud water on small-scale turbulence—laboratory model *PhD Thesis* Institute of Fundamental Technological Research, Polish Academy of Sciences (in Polish)